Harnessing ^{64}Cu/^{67}Cu for a theranostic approach to pretargeted radioimmunotherapy

Outi Keinänen[a,b], Kimberly Fung[a,c], James M. Brennan[a], Nicholas Zia[d], Matt Harris[e], Ellen van Dam[e], Colin Biggin[e], Amos Hedt[e], Jon Stoner[f], Paul S. Donnelly[d], Jason S. Lewis[b,g,h], and Brian M. Zeglis[a,b,c,g,1]

[a]Department of Chemistry, Hunter College, The City University of New York, New York, NY 10021; [b]Department of Radiology, Memorial Sloan Kettering Cancer Center, New York, NY 10065; [c]PhD Program in Chemistry, Graduate Center of the City University of New York, New York, NY 10016; [d]School of Chemistry and Bio21 Molecular Science Institute, University of Melbourne, Melbourne, VIC 3010, Australia; [e]Clarity Pharmaceuticals, Sydney, NSW 2042, Australia; [f]Idaho Accelerator Center, Idaho State University, Pocatello, ID 83201; [g]Department of Radiology, Weill Cornell Medical College, New York, NY 10021; and [h]Program in Molecular Pharmacology, Memorial Sloan Kettering Cancer Center, New York, NY 10065

Over the past decade, theranostic imaging has emerged as a powerful clinical tool in oncology for identifying patients likely to respond to targeted therapies and for monitoring the response of patients to treatment. Herein, we report a theranostic approach to pretargeted radioimmunotherapy (PRIT) based on a pair of radioisotopes of copper: positron-emitting copper-64 (^{64}Cu, $t_{1/2}$ = 12.7 h) and beta particle-emitting copper-67 (^{67}Cu, $t_{1/2}$ = 61.8 h). This strategy is predicated on the in vivo ligation between a trans-cyclooctene (TCO)-bearing antibody and a tetrazine (Tz)-based radioligand via the rapid and bioorthogonal inverse electron-demand Diels–Alder reaction. Longitudinal therapy studies were conducted in a murine model of human colorectal carcinoma using an immunoconjugate of the huA33 antibody modified with TCO (huA33-TCO) and a ^{67}Cu-labeled Tz radioligand ([^{67}Cu]Cu-MeCOSar-Tz). The injection of huA33-TCO followed 72 h later by the administration of 18.5, 37.0, or 55.5 MBq of [^{67}Cu]Cu-MeCOSar-Tz produced a dose-dependent therapeutic response, with the median survival time increasing from 68 d for the lowest dose to >200 d for the highest. Furthermore, we observed that mice that received the highest dose of [^{67}Cu]Cu-MeCOSar-Tz in a fractionated manner exhibited improved hematological values without sacrificing therapeutic efficacy. Dual radionuclide experiments in which a single administration of huA33-TCO was followed by separate injections of [^{64}Cu]Cu-MeCOSar-Tz and [^{67}Cu]Cu-MeCOSar-Tz revealed that the positron emission tomography images produced by the former accurately predicted the efficacy of the latter. In these experiments, a correlation was observed between the tumoral uptake of [^{64}Cu]Cu-MeCOSar-Tz and the subsequent therapeutic response to [^{67}Cu]Cu-MeCOSar-Tz.

theranostics | positron emission tomography | radioimmunotherapy | pretargeting | pretargeted radioimmunotherapy

Over the past decade, theranostic nuclear imaging has emerged as a valuable tool in oncology (1–4). Radiopharmaceuticals for positron emission tomography (PET) and single-photon emission computed tomography (SPECT) have increasingly been employed to identify patients who are likely to respond to targeted therapies and to monitor the response of patients to treatment. For example, PET imaging using antibodies labeled with the positron-emitting radiometal zirconium-89 (^{89}Zr; $t_{1/2} \sim 3.3$ d) has been used as a predictive tool for mesothelin- and HER2-targeted antibody-drug conjugates as well as PD-L1 checkpoint inhibitors (5–16). Theranostic imaging holds particular promise in the field of endoradiotherapy. Broadly defined, endoradiotherapy is the use of molecularly targeted agents—including small molecules, peptides, and antibodies—for the in vivo delivery of cytotoxic radiation to tumor tissue. In this context, nuclear-imaging agents can be used to select patients, monitor therapy, and optimize the safety and dosimetry of radiotherapeutics. In patients with neuroendocrine tumors, for example, [^{68}Ga]Ga-DOTA-TATE has been employed for theranostic PET imaging prior to radiotherapy with [^{177}Lu]

Lu-DOTA-TATE (LUTATHERA) (17, 18). Similarly, [^{18}F]F- and [^{68}Ga]Ga-labeled probes that target prostate-specific membrane antigen (PSMA) have been used as companion imaging agents in patients undergoing treatment with the PSMA-targeted radiotherapeutics [^{177}Lu]Lu-PSMA-617 and [^{225}Ac] Ac-PSMA-617 (19–23).

Radioimmunotherapy (RIT)—a branch of endoradiotherapy in which monoclonal antibodies are used to deliver therapeutic radionuclides to tumor tissue—has also proven to be fertile ground for theranostic imaging. To wit, antibodies labeled with the positron-emitting radionuclides ^{89}Zr, ^{86}Y, and ^{124}I have been used as companion theranostics for radioimmunoconjugates bearing therapeutic nuclides such as β-particle emitting ^{131}I, ^{90}Y, and ^{177}Lu and α-particle emitting ^{225}Ac (24–27). Yet despite their remarkable specificity and affinity, antibodies are not ideal vectors for the in vivo delivery of radionuclides, particularly those with therapeutic emissions. After administration, antibodies can take several days to accumulate in the tumor and clear from the blood, frequently requiring 5 to 10 d to reach their

---

Significance

Radioimmunotherapy is predicated on harnessing the exquisite specificity of antibodies to deliver cytotoxic radiation to tumors. Yet the long circulation time of radioimmunoconjugates leads to high radiation doses to healthy tissues. Pretargeted radioimmunotherapy (PRIT) circumvents this problem by decoupling the antibody and radionuclide, injecting the former prior to the latter, and empowering the two components to combine at the tumor. We have leveraged bioorthogonal click chemistry, a colorectal cancer-targeting antibody, and a pair radioligands bearing radioisotopes of copper—positron-emitting copper-64 and beta particle-emitting copper-67—to create a pretargeting system that enables both theranostic positron emission tomography and PRIT. We believe that the incorporation of theranostic imaging into PRIT regimens could be instrumental in the clinical success of the modality.

optimal biodistribution in the body. This means that antibodies must be labeled with radionuclides with long physical half-lives in order to ensure that sufficient radioactivity remains once the radioimmunoconjugate has reached the tumor. Several therapeutic radionuclides with multiday half-lives are readily available, including ^{177}Lu ($t_{1/2} \sim 6.7$ d), ^{131}I ($t_{1/2} \sim 8.0$ d), and ^{225}Ac ($t_{1/2} \sim 9.9$ d). Yet this combination of sluggish pharmacokinetics and long radionuclidic half-lives can lead to high radiation doses to healthy tissues, a trait which has hampered the widespread clinical implementation of RIT.

One approach to circumventing this issue is in vivo pretargeting (28–30). In vivo pretargeting is predicated on decoupling the antibody and the radionuclide, injecting the two components separately, and empowering them to combine in vivo at the tumor. More specifically, a specialized antibody capable of binding both a cancer antigen and a radiolabeled small molecule is injected first. Then, after this antibody has been given time (often several days) to accumulate in the tumor and clear from the blood, the radiolabeled small molecule is administered. This second component travels through the bloodstream quickly, either ligating with the antibody at the tumor or rapidly clearing from the body. This approach shifts the radionuclide from the immunoglobulin—where it resides during traditional immunoPET and RIT—to a rapidly clearing small molecule. As a result, a radionuclide with a multiday physical half-life is no longer needed, a change which simultaneously facilitates the use of short-lived nuclides that are normally incompatible with antibodies and reduces radiation dose rates to healthy tissues.

Over the last several years, our laboratories and others have developed an approach to in vivo pretargeting based on the rapid and bioorthogonal inverse electron-demand Diels–Alder click reaction between trans-cyclooctene (TCO) and tetrazine (Tz) (Fig. 1A) (31–36). Broadly speaking, this methodology consists of four steps: 1) the administration of a monoclonal antibody (mAb)-TCO immunoconjugate; 2) an interval period during which the antibody accumulates at the tumor and clears from the blood; 3) the injection of a small molecule Tz-based radioligand; and 4) the in vivo click ligation between two components, followed by the rapid clearance of any excess radioligand. This strategy has proven highly effective for pretargeted PET imaging (36–49) as well as pretargeted radioimmunotherapy (PRIT) using beta-emitting (^{177}Lu) and alpha-emitting (^{225}Ac) radionuclides (50–55). Yet as the field stands poised to make the jump from the laboratory to the clinic, it stands to reason that the development of a theranostic approach to Tz/TCO pretargeting could prove instrumental in ensuring the future success of this modality.

Herein, we report a theranostic approach to in vivo pretargeting that incorporates both PET imaging and radioimmunotherapy. In this case, the administration of the mAb-TCO immunoconjugate is followed by the sequential injection of two Tz-bearing radioligands: one for theranostic PET and a second for endoradiotherapy (Fig. 2). The key to this investigation is a pair of radioisotopes of copper that allows us to create radioligands that are completely identical except for the number of neutrons within the copper atom: copper-64 (^{64}Cu, $t_{1/2} = 12.7$ h) and copper-67 (^{67}Cu, $t_{1/2} = 61.8$ h) (Fig. 1B). While ^{64}Cu is a relatively well-known positron-emitting nuclide, ^{67}Cu produces beta particles ($\beta_{ave} = 141$ keV) that are suitable for endoradiotherapy as well as gamma rays (185 keV, 49%; 93 keV, 16%) that can be imaged via SPECT. For years, challenges in the large-scale production of ^{67}Cu have impeded its use in nuclear medicine, although recent advances are expected to dramatically increase its availability (56, 57). Furthermore, the advent of highly stable copper chelators based on bicyclo[6.6.6] icosane—termed "sarcophagines"—has also reinvigorated interest in ^{67}Cu as a therapeutic radionuclide, as illustrated by the recent development of [$^{64/67}$Cu]Cu-SarTATE for the PET imaging and peptide receptor radiotherapy of patients with neuroendocrine tumors (58–61).

To provide a bird's-eye view of the investigation, we first synthesized and characterized the two radioligands—[^{64}Cu]Cu-MeCOSar-Tz and [^{67}Cu]Cu-MeCOSar-Tz—as well as a TCO-bearing immunoconjugate of the huA33 antibody, a noninternalizing humanized mAb that targets a transmembrane glycoprotein (i.e., the A33 antigen) expressed by the vast majority of colorectal cancers (62–65). HuA33-TCO and [^{67}Cu]Cu-MeCOSar-Tz were then employed to perform biodistribution and longitudinal therapy studies in a murine model of colorectal cancer in order to determine the dosimetry and validate the efficacy of ^{67}Cu-based PRIT. Finally, in vivo pretargeting experiments were performed using huA33-TCO in conjunction with both radioligands to interrogate the therapeutic efficacy of the dual isotope strategy as well as the predictive value of theranostic PET in this schema. We have demonstrated that this innovative approach to PRIT is highly effective in vivo and may thus furnish a roadmap for how theranostic imaging may be used to supplement this methodology in the clinic. Our approach to in vivo pretargeting employs an isotopologous pair of radioligands for theranostic PET imaging and endoradiotherapy. This is absolutely critical in the context of clinical translation, as the use of a single, structurally unique radioligand—rather than two chemically distinct constructs labeled with different radioelements—will simplify the collection of pharmacology and toxicology data and streamline the regulatory review process.

Materials and Methods

All reagents were purchased from commercial suppliers and used without further purification. All experiments involving laboratory animals were performed in accordance with a protocol approved by Hunter College, Weill Cornell Medical College, and Memorial Sloan Kettering Cancer Center
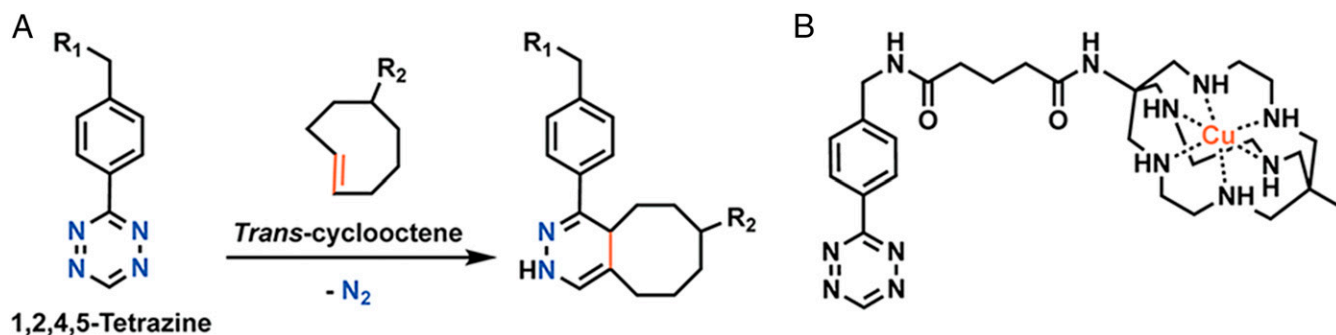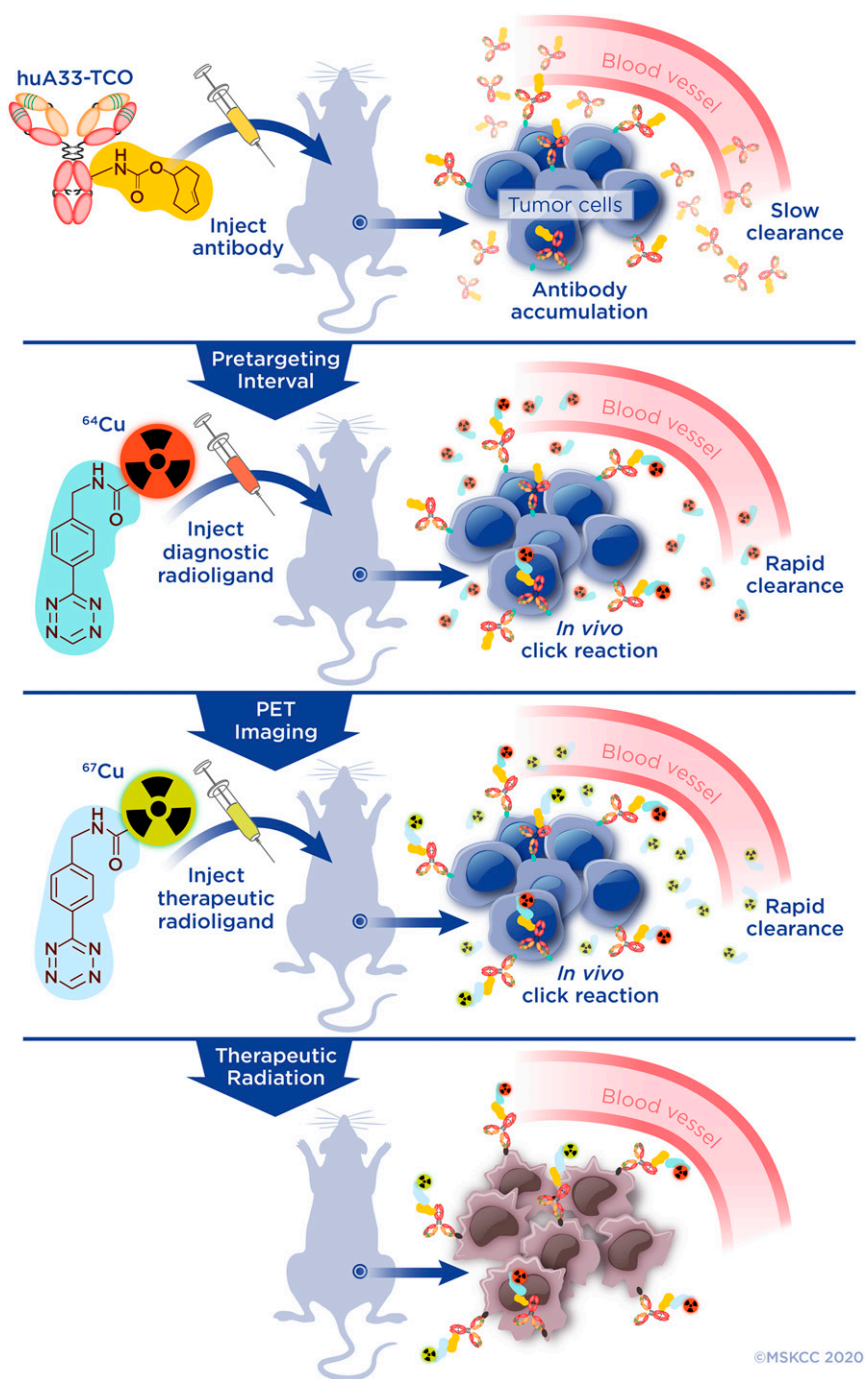
Fig. 1. (A) The inverse electron demand Diels–Alder (IEDDA) reaction between trans-cyclooctene and tetrazine. (B) The structure of Cu-MeCOSar-Tz.

Fig. 2. PRIT. Illustration of the theranostic approach to PRIT. The immunoconjugate (huA33-TCO) is injected first and given time to slowly accumulate at the tumor and clear from the blood. After this interval, the ^{64}Cu-labeled radioligand is injected. It then clicks with the huA33-TCO at the tumor and clears rapidly from the blood, enabling theranostic PET imaging. Next, the ^{67}Cu-labeled radioligand is administered, and it likewise is given time to react with the tumor-bound immunoconjugate and clear from the system, thus beginning the therapeutic irradiation of the tumor tissue. PRIT can be performed without theranostic imaging by omitting the administration of the diagnostic radioligand.

Institutional Animal Care and Use Committees. A detailed description of experimental procedures—including synthetic protocols, bioconjugation techniques, radiolabeling methodologies, and the design and execution of in vivo experiments—can be found in the *SI Appendix*.

Synthesis of MeCOSar-Tz. MeCOSar-NHS was prepared as previously described (66, 67). Briefly, to a solution of MeCOSar-NHS (0.053 mmol) in dimethylformamide (DMF; 530 μL) was added benzylaminotetrazine hydrochloride (11.8 mg, 0.053 mmol) and diisopropylethylamine (18.4 μL, 0.11 mmol).

The reaction volume of the reaction mixture was increased to 1 mL with DMF, and the reaction was stirred for 1 h at 60 °C in the absence of light. The product—MeCOSar-Tz—was purified by reversed-phase high performance liquid chromatography (HPLC). Analysis of the fractions by HPLC-electrospray ionization mass spectrometry (ESI-MS) identified those containing the product, and these fractions were lyophilized to afford MeCOSar-Tz·CF$_3$CO$_2$ as a fluffy pink powder (12 mg, ~38%), ESI-MS $[C_{29}H_{49}N_{12}O_{22}]^+ = 597.410$; $[C_{29}H_{50}N_{12}O_{22}]^{2+} = 299.208$; HPLC R$_T$ = 13.8 min, 0 to 25% solvent B [solvent A: H$_2$O, 0.1% trifluoroacetic acid (TFA); solvent B: CH$_3$CN, 0.1% TFA] over 25 min.

Radiolabeling of MeCOSar-Tz. MeCOSar-Tz was radiolabeled with $[^{64}Cu]Cu^{2+}$ or $[^{67}Cu]Cu^{2+}$ by diluting the stock solution (0.36 mg/mL in dimethylsulfoxide) into ammonium acetate buffer (200 mM, pH 5.5, 200 to 300 μL) prior to the addition of $[^{64}Cu]CuCl_2$ in 0.05 M HCl or $[^{67}Cu]CuCl_2$ in 0.01 M HCl. The labeling solution was incubated on an agitating thermomixer at $500 \times g$ for 20 min at 37 °C. The progress of the radiolabeling reaction was assessed via instant thin layer chromatography (iTLC), which revealed quantitative labeling with >99% radiochemical purity. Thus, no further purification was necessary.

Tumor Model. All in vivo studies were carried out in female, athymic nude mice (5 to 7 wk old, The Jackson Laboratory). Mice were xenografted subcutaneously (s.c.) on the right flank with 5×10^6 SW1222 cells suspended in 150 μL of a solution containing a 1:1 mixture of Matrigel (Corning Life Sciences) and cell culture medium. The tumors reached the ideal size for experiments (~100 mm³) after ~14 d.

Ex Vivo Biodistribution Experiments. For pretargeting biodistribution experiments, the mice were injected via the lateral tail vein with huA33-TCO (100 μg, 0.7 nmol, 5 TCO/mAb) 24 or 72 h prior to the intravenous (i.v.) administration of $[^{67}Cu]Cu$-MeCOSar-Tz (9.5 to 11.0 MBq, 0.7 to 0.8 nmol). In contrast, a control cohort of mice received only $[^{67}Cu]Cu$-MeCOSar-Tz (9.3 to 10.0 MBq, 0.7 nmol). At 4, 24, 48, and 72 h after the injection of $[^{67}Cu]Cu$-MeCOSar-Tz, the mice were killed, and their organs were collected, weighed, and assayed for radioactivity with a gamma counter calibrated for ^{67}Cu using known standards.

In biodistribution experiments with directly radiolabeled huA33, $[^{67}Cu]Cu$-MeCOSar-Tz-TCO-huA33 (1.9 MBq, 100 μg, 0.7 nmol) was administered via i.v. tail-vein injection. At 4, 24, 72, and 120 h post injection, the mice were killed, and their organs were collected, weighed, and assayed for radioactivity with a gamma counter calibrated for ^{67}Cu using known standards.

Dosimetry Calculations. The average activity concentration from five tissue samples from each time point was fitted to a biexponential function to create time-activity curves (TAC). For most tissues, the best TAC fit utilized a one- or two-phase exponential decay model. One tissue—the tumor—exhibited marked uptake over the time course of the experiment, and, therefore, a trapezoidal model was used up to the last time point, after which it was assumed (due to the residualizing nature of $[^{67}Cu]Cu^{2+}$) that clearance was determined entirely by radioactive decay. The cumulative uptake in each tissue was calculated from the areas under the time-activity curves. Absorbed doses to the tumor and all healthy organs were estimated assuming absorbed fractions of 1 for the β-emissions of ^{67}Cu and of 0 for the penetrating photon emissions and using an equilibrium absorbed dose constant of 0.33 g × Rad/μCi × h.

Longitudinal Radiotherapy Studies. In the longitudinal radiotherapy studies, three control cohorts, four PRIT cohorts, one theranostic PRIT cohort, and one traditional RIT cohort were employed ($n = 10$). The first control cohort received only saline, the second received only huA33-TCO (100 μg, 0.7 nmol, 5 TCO/mAb), and the third received only $[^{67}Cu]Cu$-MeCOSar-Tz (55.5 MBq, 0.7 nmol). The injection day was designated "day 0" of the experiment.

Based on the biodistribution data for pretargeting with huA33-TCO and $[^{67}Cu]Cu$-MeCOSar-Tz, the 72-h injection interval was chosen for the longitudinal therapy study because it produced lower activity concentrations in the blood. All animals in the PRIT cohorts were administered huA33-TCO (100 μg, 0.7 nmol, 5 TCO/mAb) followed 72 h later by the injection of $[^{67}Cu]Cu$-MeCOSar-Tz (18.5, 37, 55.5, or 27.8 MBq, 0.7 nmol, day 0). To explore the efficacy of fractioned dosing, the group receiving 27.8 MBq was administered a second dose of 27.8 MBq (0.7 nmol) 48 h later. SPECT imaging was carried out at 4, 24, 48, and 96 h post injection.

In the theranostic PRIT cohort, the mice were administered $[^{64}Cu]Cu$-MeCOSar-Tz (10.4 to 11.3 MBq, 0.7 nmol, day 0) at the 72-h time point, followed 24 h later by $[^{67}Cu]Cu$-MeCOSar-Tz (55.5 MBq, 0.7 nmol). PET imaging was performed at 4, 24, and 48 h after the injection of $[^{64}Cu]Cu$-MeCOSar-Tz. The activity within each tumor was determined using PET image slices acquired at 48 h after the administration of the ^{64}Cu-labeled radioligand and subsequently compared to the rate of tumor growth. SPECT imaging was carried out at 4, 24, 48, and 96 h post injection of $[^{67}Cu]Cu$-MeCOSar-Tz. In the RIT cohort, the mice were administered $[^{67}Cu]Cu$-MeCOSar-Tz-TCO-huA33 (18.5 MBq, 100 μg, 0.7 nmol, day 0), and SPECT imaging was carried out at 4, 24, 48, and 96 h post injection.

The volumes of the xenografts were monitored twice a week with a Peira TM900 device. All mice were assessed biweekly throughout the study for outward signs of toxicity, including lethargy, loss of appetite, and decreasing body weight. Five possible end points of the study were defined: 1) if the longest dimension of the tumor reached 1 cm; 2) if the tumor started to hamper the movement of the mouse; 3) if the tumor became necrotic; 4) if the mouse lost more than 10% of its body weight; or 5) after 200 d. Blood samples (~30 μL, $n = 3$) were collected weekly from the lateral tail vein and analyzed with HemaVet 950 (Drew Scientific). Twenty hematological parameters were measured, including white-blood-cell count and platelet count.

Statistical Analysis. All data are reported as mean value ± SD. The significance analyses were performed using GraphPad Prism 7.0 software. Unpaired two-tailed t tests, multiple t tests, or a log-rank Mantel-Cox test were employed as detailed in the figure legends.

Results

Bioconjugation, Synthesis, and Radiochemistry. The first step of the investigation was the assembly of the molecular components of our in vivo system. To this end, huA33-TCO was synthesized according to published procedures via the reaction of an N-hydroxysuccinimide–bearing variant of TCO with the parent antibody, ultimately producing the immunoconjugate with a degree of labeling of 5.2 ± 0.1 TCO/mAb and an immunoreactivity of $88.9 \pm 1.8\%$ ($n = 5$) as determined via matrix-assisted laser desorption ionization time-of-flight mass spectrometry and in vitro saturation binding assays, respectively. Size exclusion-HPLC was performed to validate the purity of huA33-TCO and confirmed that no significant aggregation had occurred during the bioconjugation process (*SI Appendix*, Fig. S1). For the radioligand, we paired Tz with MeCOSar, a member of the sarcophagine family that exhibits exceptional in vitro and in vivo stability as a chelator for the radioisotopes of copper (58–61, 67–69). MeCOSar-Tz was synthesized and purified according to published procedures and isolated with a yield of ~38%. The radiolabeling of MeCOSar-Tz was performed identically with both radioisotopes via the incubation of the precursor with $[^{64}Cu]CuCl_2$ or $[^{67}Cu]CuCl_2$ in ammonium acetate buffer (200 mM, pH 5.5) for 20 min at 37 °C. $[^{64}Cu]Cu$-MeCOSar-Tz was ultimately isolated in quantitative radiochemical yield, a radiochemical purity of >99%, and a molar activity of 15.3 to 16.5 GBq/μmol, while $[^{67}Cu]Cu$-MeCOSar-Tz was produced in quantitative radiochemical yield, a radiochemical purity of >99%, and a molar activity of 74.1 to 82.3 GBq/μmol. It is important to note that in all of the in vivo pretargeting experiments performed in this investigation, the molar activity of the radioligand was adjusted to ensure that each injection contained 0.7 nmol of Tz, as a 1:1 ratio of immunoconjugate:radioligand has been shown to provide superior in vivo results compared to approaches that use a vast excess of either component (70). Finally, $[^{67}Cu]Cu$-MeCOSar-huA33 was synthesized in order to provide a directly radiolabeled antibody control for the biodistribution and longitudinal therapy experiments. $[^{67}Cu]Cu$-MeCOSar-Tz was reacted with huA33-TCO for 0.5 h at 37 °C, and the reaction solution was purified via size exclusion chromatography (Sephadex G-25M, PD-10 column, GE Healthcare; dead volume: 2.5 mL, eluted with 2 mL of phosphate-buffered saline, pH 7.4) to provide the final radioimmunoconjugate in an isolated radiochemical yield of 49%, a radiochemical purity of >99%, and a specific activity of 32.1 GBq/μmol.

Ex Vivo Biodistribution. With the synthesis and characterization of the components complete, the next step was to evaluate the in vivo performance of the system. But before we could move on to the dual isotope theranostic strategy, it was critical to first establish the efficacy of PRIT with huA33-TCO and $[^{67}Cu]Cu$-MeCOSar-Tz alone. This process began with pretargeted biodistribution experiments designed to probe the pharmacokinetic profile of $[^{67}Cu]Cu$-MeCOSar-Tz, determine the optimal interval time between the injections of immunoconjugate and radioligand, and facilitate the calculation of the radiation dose rates to

the tumor and healthy organs. To this end, athymic nude mice bearing s.c. A33 antigen-expressing SW1222 human colorectal carcinoma xenografts were administered huA33-TCO (100 μg, 0.7 nmol) and then—following an interval of either 24 or 72 h—[⁶⁷Cu]Cu-MeCOSar-Tz (9.3 to 10.0 MBq, 0.7 nmol). In addition, a control arm of the experiment was performed in which tumor-bearing mice were administered the same dose of [⁶⁷Cu]Cu-MeCOSar-Tz alone. After 4, 24, 48, and 72 h, the cohorts ($n = 5$ per time point) were killed, and the tumor as well as selected organs were harvested, washed, dried, and assayed for ⁶⁷Cu on a gamma counter (Fig. 3A and *SI Appendix*, Tables S1–S3).

In the absence of huA33-TCO, [⁶⁷Cu]Cu-MeCOSar-Tz cleared quickly from the blood and healthy organs, was eliminated via the urine, and produced negligible tumoral uptake (i.e., 0.2 ± 0.1%ID/g at 72 hours post injection [h.p.i.]). In contrast, high-activity concentrations in the tumor were observed in the mice treated with both huA33-TCO and [⁶⁷Cu]Cu-MeCOSar-Tz, with values reaching 10.2 ± 2.1%ID/g (24-h interval) and 9.2 ± 1.3%ID/g (72-h interval) at 72 h.p.i. In these same mice, the residual activity concentration in the blood decreased over the course of the experiment, starting around 3 to 4%-ID/g at 4 h.p.i. and reaching 0.5 to 1.0%ID/g at 120 h.p.i. The uptake in other tissues remained relatively low throughout the study, with the liver the healthy organ with the highest level of uptake (∼1 to 3%ID/g). Taken together, these numbers produce high tumor-to-healthy organ activity concentration ratios, e.g., tumor-to-blood, -muscle, -liver, and -large intestine ratios of 20.2 ± 7.7, 159.2 ± 35.6, 6.0 ± 1.6, and 66.8 ± 37.7 at 120 h.p.i. for the cohort with a 72-h injection interval.

Dosimetry. Radiation dose rates and therapeutic indices for both pretargeting intervals were calculated from the biodistribution data (Fig. 3B). In addition, a biodistribution experiment was performed with directly labeled [⁶⁷Cu]Cu-huA33 and employed for dosimetry calculations (*SI Appendix*, Fig. S2 and Table S4). As expected, both pretargeting approaches yielded reductions in radiation dose rates compared to the directly radiolabeled antibody. For example, the pretargeting strategy with a 72-h interval produces dose rates of 5.9 and 14.2 cGy/MBq to the blood and liver, respectively, while [⁶⁷Cu]Cu-huA33 creates dose rates of 72.3 and 111.5 cGy/MBq to the same organs. However, significant decreases in the radiation dose rates to the tumor in the pretargeting cohorts (63.0 and 57.2 cGy/MBq for 24-h and 72-h intervals, respectively) compared to the cohort that received the directly labeled antibody (574.5 cGy/MBq) mean that the therapeutic indices—i.e., the ratios of the radiation dose rates to the tumor to the radiation dose rates to specific healthy tissues—for all three methodologies lie in similar ranges. To wit, while pretargeting with a 24-h interval produces a tumor-to-blood therapeutic index (6.5) below that of the directly labeled antibody (8.1), the pretargeting strategy with a 72-h interval yields the highest therapeutic index (9.7) of all three. In the end, given its higher tumor-to-blood therapeutic index, the 72-h PRIT strategy was selected for longitudinal therapy studies.

Longitudinal Radiotherapy. Longitudinal radiotherapy studies were performed to interrogate the efficacy and safety of this approach to PRIT. These experiments initially employed eight different cohorts ($n = 10$) of mice bearing s.c. SW1222 human colorectal cancer xenografts (Fig. 4A). The three PRIT cohorts received huA33-TCO (100 μg, 0.7 nmol) followed 72 h later by three different doses of [⁶⁷Cu]Cu-MeCOSar-Tz: 18.5, 37.0, or 55.5 MBq (in each case, 0.7 nmol). In contrast, the three control cohorts received the vehicle (0.9% sterile saline) alone, huA33-TCO alone, or [⁶⁷Cu]Cu-MeCOSar-Tz alone (55.5 MBq). In order to probe the value of fractionated dosing, a seventh cohort received huA33-TCO (100 μg, 0.7 nmol) followed 72 h later by

two 27.8-MBq doses of [⁶⁷Cu]Cu-MeCOSar-Tz separated by 48 h. Finally, an eighth, "traditional RIT" cohort received a single dose of [⁶⁷Cu]Cu-MeCOSar-Tz-TCO-huA33 (18.5 MBq).

While the growth of the tumors in the control cohorts continued unabated throughout the study, the tumors within the mice of the PRIT and RIT cohorts exhibited a short initial period of growth followed by a dramatic reduction in volume (Fig. 4B). Indeed, all of the mice in the radiotherapy cohorts ultimately reached a point at which their xenografts were smaller than they had been on day 0. A dose-dependent therapeutic response was observed among the three single-dose PRIT cohorts, with the group receiving 55.5 MBq of [⁶⁷Cu]Cu-MeCOSar-Tz exhibiting the most significant regrowth delay. Similar regrowth delay was found in the mice that received 18.5 MBq of the conventional radioimmunoconjugate, [⁶⁷Cu]Cu-huA33. Finally, the response of the mice receiving fractionated PRIT largely mirrored that of the 55.5-MBq PRIT cohort.

The efficacy of each treatment regimen is most clearly visualized using a Kaplan–Meier plot (Fig. 4C). The median survival times of the control cohorts are 21 d (vehicle only), 21 d (huA33-TCO only), and 31.5 d ([⁶⁷Cu]Cu-MeCOSar-Tz only). These values stand in stark contrast to the median survival times of the cohorts that received treatment: 68.5 d (single-dose PRIT, 18.5 MBq), 98.5 d (single-dose PRIT, 37.0 MBq), 200 d (single-dose PRIT, 55.5 MBq), 189 d (fractionated-dose PRIT), and 200 d (RIT). Statistical analysis of the data confirms significant differences (P values < 0.01) between the control groups and all of the radiotherapy cohorts as well as between the 18.5 and 37.0 MBq PRIT cohorts and the remaining three experimental groups. No statistically significant differences exist, however, between the survival of the 55.5-MBq PRIT, fractionated PRIT, and traditional RIT cohorts. While the vast majority of the mice killed during the study had tumors that exceeded the maximum permissible size, a handful of animals had to be killed—or were found dead—due to other pathologies (*SI Appendix*, Table S5). In light of the dosimetry data, body-weight measurements, and blood analysis (see *Body Weight and Blood Analyses* below), it is unlikely that these events stemmed from the endoradiotherapy itself but rather were related to the aging of the immunocompromised mice.

SPECT Imaging. In addition to its therapeutic 141-keV β-particle, ⁶⁷Cu also emits 185 keV (49%) and 93 keV (16%) gamma rays that are suitable—although admittedly suboptimal—for SPECT imaging. In order to probe the possibility of exploiting these emissions to visualize the ⁶⁷Cu-based therapies, SPECT imaging was carried out for each cohort at 4, 24, 48, and 96 h after the administration of radioactivity (Fig. 5 and *SI Appendix*, Fig. S3). Fig. 5 contains representative SPECT maximum intensity projections (MIPs) from three cohorts: 55.5-MBq single-dose PRIT, fractioned-dose PRIT (27.8 + 27.8 MBq), and RIT (18.5 MBq). In the mice receiving fractionated doses of PRIT, the second dose of [⁶⁷Cu]Cu-MeCOSar-Tz was administered after the 48-h SPECT scan, and the mice were imaged again 4 h (52 h after the first dose) and 48 h (96 h after the first dose) later. Taken together, these images illustrate several trends. First, the excretion of free [⁶⁷Cu]Cu-MeCOSar-Tz through the urinary tract can be clearly visualized in the images collected at 4 h.p.i. Second, in all of the cohorts, the tumor is the tissue with the highest activity concentration after 24 h. Third, the tumoral activity concentration in the cohort receiving fractioned PRIT increases following the administration of the second dose, underscoring the viability of this approach. Finally, as expected, the cohort that was administered directly labeled [⁶⁷Cu]Cu-huA33 exhibited elevated activity concentrations in the liver compared to the PRIT groups.

Body Weight and Blood Analyses. In order to assess the potential toxicity of this methodology, the body weight of each animal was measured twice per week. All of the mice—except for one in the
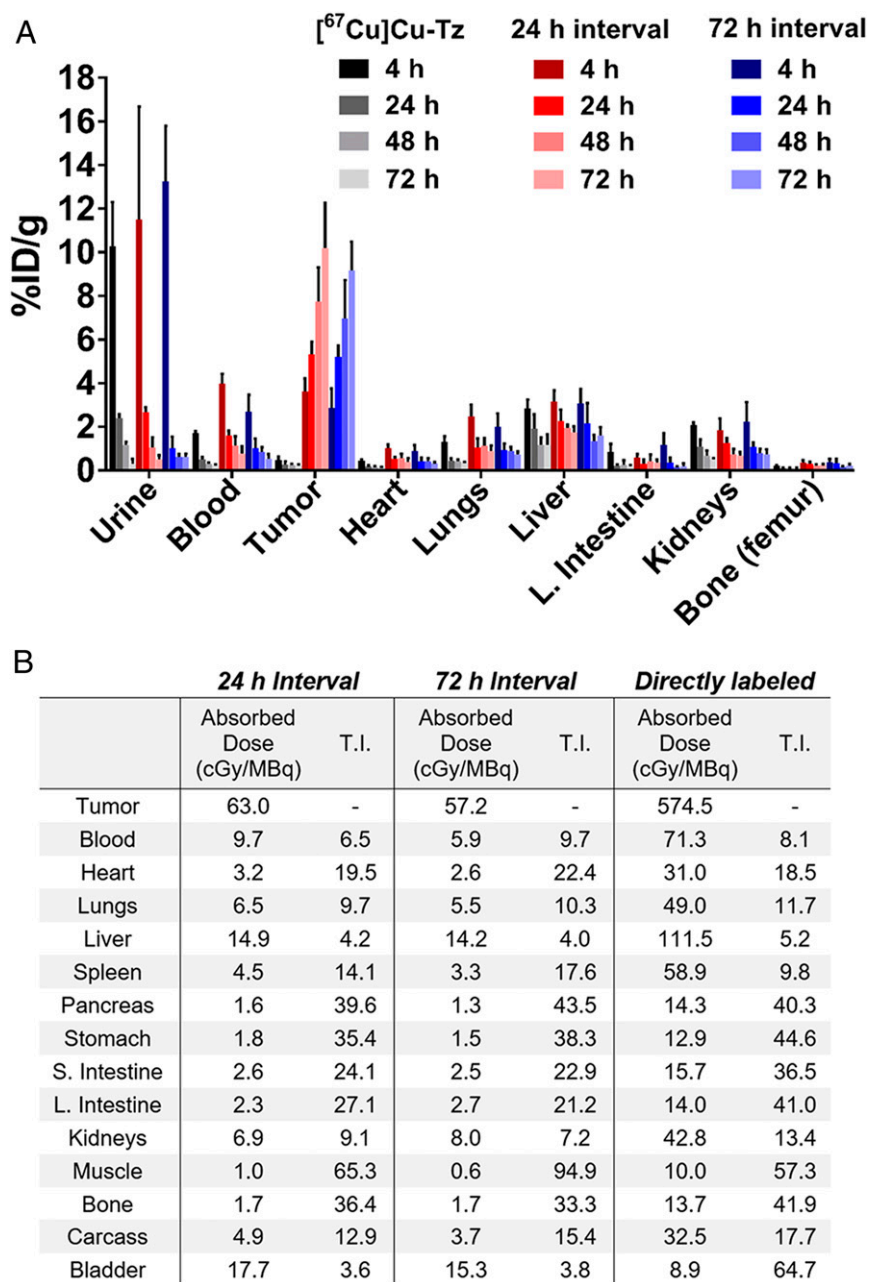
Fig. 3. Biodistribution and dosimetry data. (*A*) Biodistribution data in athymic nude mice bearing s.c. SW1222 xenografts for [^{67}Cu]Cu-MeCOSar-Tz ([^{67}Cu]Cu-Tz, 9.3 to 10.0 MBq, 0.7 nmol) alone as well as in vivo pretargeting using [^{67}Cu]Cu-MeCOSar-Tz and huA33-TCO with 24- and 72-h injection intervals. For the latter, the mice were first administered huA33-TCO (100 μg, 0.7 nmol, 5 TCO/mAb) i.v. via the tail vein, followed 24 or 72 h later by the i.v. administration of [^{67}Cu]Cu-MeCOSar-Tz (9.5 to 11.0 MBq, 0.7 to 0.8 nmol). (*B*) Dosimetry data derived from the biodistribution data shown as well as biodistribution data for directly labeled [^{67}Cu]Cu-MeCOSar-Tz-TCO-huA33 (1.9 MBq, 100 μg, 0.7 nmol, n = 5) in athymic nude mice bearing s.c. SW1222 xenografts collected 4, 24, 72, and 120 h.p.i. The data are presented as mean values ± SDs (n = 5); stomach, small intestine, and large intestine values include the contents. T.I.: therapeutic index.

control cohort that received huA33-TCO only—maintained an acceptable body weight (>90% of original weight) throughout the course of the study (Fig. 6*A*). During the first 2 wk, slight decreases were observed in the body weight of the mice in the [^{67}Cu]Cu-MeCOSar-Tz only, 55.5-MBq PRIT, fractioned-dose PRIT, and RIT cohorts, but this trend self-corrected soon thereafter. Generally speaking, however, the average weight loss did not exceed 5% for any of the radiotherapy cohorts, suggesting that this approach was well tolerated up to the highest doses tested.

In addition to monitoring the weight of the animals, an analysis of the blood of representative mice from each cohort was performed weekly (Fig. 6*B* and *SI Appendix*, Fig. S4). White blood cell (WBC) counts decreased initially in all of the cohorts that received doses of ^{67}Cu, although these values recovered over the course of the experiment (Fig. 6*B*). The largest drop was observed in the 55.5-MBq single-dose PRIT cohort. Interestingly, when 55.5 MBq of [^{67}Cu]Cu-MeCOSar-Tz was delivered as a fractioned dose—i.e., two doses of 27.8 MBq separated by 2 d—a smaller decrease in the WBC count occurred (*P* = 0.01
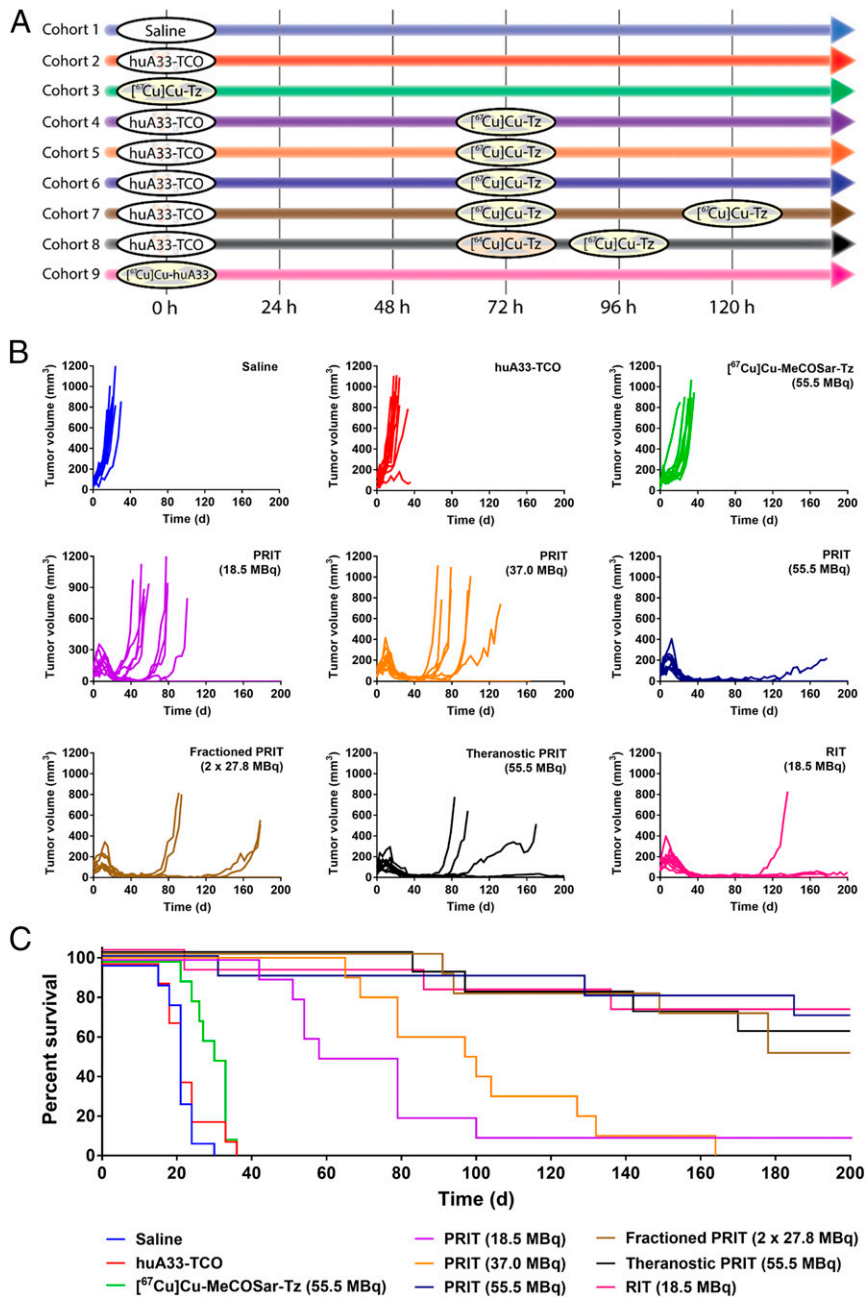
Fig. 4. Longitudinal radiotherapy study in mice bearing s.c. SW1222 xenografts. (*A*) Experimental timelines for each cohort. (*B*) Tumor volumes of the individual mice of each cohort as a function of time. (*C*) Kaplan–Meier plot depicting the survival of the mice of each cohort. Median survivals: 21 d (saline only; blue); 21 d (huA33-TCO only; red); 31.5 d ([^{67}Cu]Cu-MeCOSar-Tz only; green); 68.5 d (18.5-MBq PRIT, purple); 98.5 d (37.0-MBq PRIT, orange); 200 d (55.5-MBq PRIT, dark blue); 189 d (fractioned-dose PRIT, brown); 200 d (theranostic PRIT, black); and 200 d (RIT, pink). *P* values for median survival: 1/2/3 vs. 4/5/6/7/8 and 1/2 vs. 9 < 0.0001; 3 vs. 9 = 0.0002; 4 vs. 5 = 0.29; 4 vs. 6 = 0.0025; 4 vs. 7 = 0.0022; 4 vs. 8 = 0.0014, 4 vs. 9 = 0.0035; 5 vs. 6 = 0.0003; 5 vs. 7 = 0.0008; 5 vs. 8 = 0.0007; 5 vs. 9 = 0.0014; 6 vs. 7 = 0.40; 6 vs. 8 = 0.65; 6 vs. 9 = 0.94; 7 vs. 8 = 0.79; 7 vs. 9 = 0.54; 8 vs. 9 = 0.76. The significance analyses were performed with GraphPad Prism 7.0 software using the log-rank Mantel–Cox test.

at day 7). The RIT cohort, not surprisingly, exhibited a more substantial drop—and a more sluggish recovery—in WBC count than the PRIT cohort that received the same dose of radioactivity (18.5 MBq). Platelet counts likewise dropped for all of the cohorts that received ^{67}Cu, but the most significant decrease occurred in the 55.5-MBq PRIT cohort (Fig. 6*B*). Furthermore, a more substantial decrease in platelet count was again observed in the cohort receiving RIT compared to the group receiving an equal dose of PRIT (*P* = 0.001 at day 14). Like the WBC counts, however, the decreased platelet count

values recovered in all of the cohorts after the first 3 wk of the study.

Incorporating Theranostic PET Imaging into ^{67}Cu-PRIT. The final step in the investigation was the in vivo evaluation of a dual isotope approach to PRIT that incorporates ^{64}Cu-based PET imaging as well as ^{67}Cu-based endoradiotherapy. To this end, a longitudinal therapy experiment was performed in which athymic nude mice bearing s.c. A33 antigen-expressing SW1222 were given three injections: huA33-TCO (100 µg, 0.7 nmol), followed 72 h later by
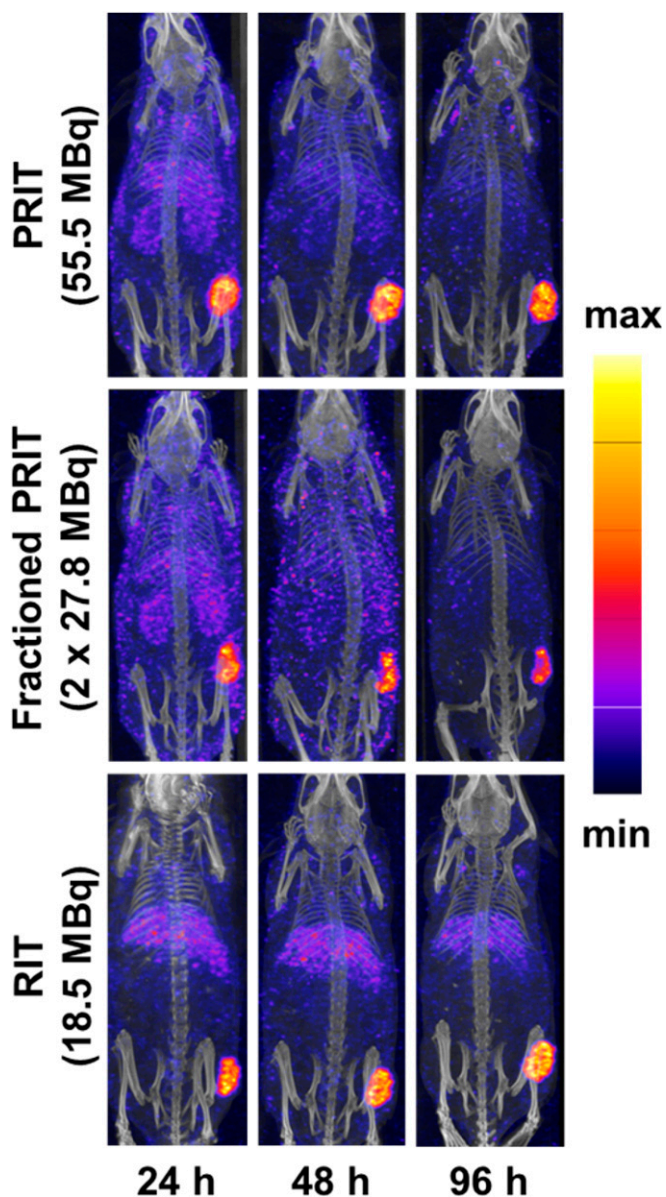
Fig. 5. SPECT-computed tomography MIP images of representative mice from the cohorts treated with (*Top*) 55.5-MBq PRIT, (*Middle*) fractionated PRIT, and (*Bottom*) RIT. The second dose in the fractioned PRIT cohort was administered immediately after the collection of the 48-h SPECT scan. The mice were then imaged again 48 h later (corresponding to 96 h after the first dose of radioligand).

$[^{64}Cu]$Cu-MeCOSar-Tz (10.4 to 11.3 MBq, 0.7 nmol), followed 24 h later by $[^{67}Cu]$Cu-MeCOSar-Tz (55.5 MBq, 0.7 nmol) (Fig. 7*A*). From a therapeutic perspective, this approach produced a mean survival of >200 d and tumor growth arrest comparable to the three most effective therapeutic strategies: 55.5-MBq PRIT, fractionated PRIT, and RIT (Fig. 4). PET images collected at 4, 24, and 48 h after the administration of the ^{64}Cu-labeled radioligand reflect our previous findings, with the tumor tissue clearly visible at early time points and becoming far and away the most prominent feature by 24 and 48 h.p.i (Fig. 7*B*). Not surprisingly, the PET images collected at 48 h.p.i. revealed heterogeneity in the tumoral uptake of $[^{64}Cu]$Cu-MeCOSar-Tz, with radioactivity levels in the center of the xenograft ranging from 3.0 to 12.6 kBq. Importantly, the therapeutic responses of individual mice seem to correlate with the level of

uptake of $[^{64}Cu]$Cu-MeCOSar-Tz in the tumor (Fig. 7*C*). To wit, the four mice that experienced tumor regrowth were the four mice with the lowest uptake of $[^{64}Cu]$Cu-MeCOSar-Tz in the tumor: 3.0, 4.1, 5.6, and 6.8 kBq. In contrast, the six mice with higher levels of $[^{64}Cu]$Cu-MeCOSar-Tz in the tumor—all >9.0 kBq—exhibited complete tumor remission. Finally, the SPECT images obtained from $[^{67}Cu]$Cu-MeCOSar-Tz closely mirror the PET images, reinforcing the theranostic value of the latter (Fig. 7*D*).

Discussion

Radioimmunoconjugates have long held promise for targeted endoradiotherapy, yet their widespread clinical implementation has been hindered due to concerns over their high radiation dose rates to healthy tissues. In recent years, theranostic imaging has helped clinicians select patients for RIT and optimize the dose of radioimmunoconjugates to maximize their safety and efficacy. And, while the advent of companion imaging agents has undoubtedly moved the field forward, it has not eliminated the intrinsic problems of radiolabeled antibodies.

The overarching goal of this investigation was to create a pretargeted approach to endoradiotherapy capable of leveraging the advantages of antibodies and theranostic imaging while simultaneously skirting the pharmacokinetic—and, consequently, dosimetric—limitations of full-length immunoglobulins. Over the past 5 years, our laboratories have developed a strategy for in vivo pretargeting based on the rapid and bioorthogonal inverse electron-demand Diels–Alder ligation between a TCO-bearing immunoconjugate and a Tz-containing radioligand. We have confirmed the efficacy of this approach in several murine models of cancer using a variety of different antibodies and positron-, β-, and α-emitting radionuclides, including ^{18}F, ^{68}Ga, ^{177}Lu, and ^{225}Ac. Yet until recently, each of these demonstrations focused on only a single modality: PET or PRIT.

As we shifted our attention to a theranostic approach to pretargeting, it became apparent that we would need to employ either a single radionuclide with emissions suitable for both imaging and therapy or a pair of radionuclides, each with emissions suitable to one of the two tasks. Given that the former are few and far between, we turned to the use of a radionuclide pair. Along these lines, we demonstrated the feasibility of dual-isotope pretargeting using ^{64}Cu- and ^{177}Lu-labeled tetrazines: $[^{64}Cu]$Cu-SarAr-Tz and $[^{177}Lu]$Lu-DOTA-PEG$_7$-Tz (48). Without question, the single most important finding of this work is that the injection of a first radioligand does not adversely affect the tumoral uptake or overall biodistribution of a second radioligand. To wit, in pretargeting experiments using a 48-h interval between the administration of huA33-TCO and $[^{177}Lu]$Lu-DOTA-PEG$_7$-Tz, activity concentrations of 5.2 ± 1.2, 9.0 ± 2.6, and $13.0 \pm 2.8\%ID/g$ were observed in the tumor at 4, 24, and 48 h.p.i. Under identical conditions—but with the injection of $[^{64}Cu]$Cu-SarAr-Tz a day after the immunoconjugate and a day before the ^{177}Lu-labeled radioligand—the tumoral activity concentrations of $[^{177}Lu]$Lu-DOTA-PEG$_7$-Tz were found to be all but identical: 4.9 ± 0.4, 11.3 ± 1.6, and $13.1 \pm 2.7\%ID/g$ at the same time points. This phenomenon is of paramount importance in the context of theranostics, as it ensures that a radioligand administered for imaging does not attenuate the uptake or efficacy of a radioligand administered for therapy (48, 52). Yet this $^{64}Cu/^{177}Lu$-based strategy is ultimately suboptimal from a theranostic standpoint because the two radioligands are different and thus will exhibit different pharmacokinetic profiles and in vivo behavior. Furthermore, the use of ^{177}Lu ($t_{1/2} \sim 6.7$ d) fails to take advantage of an important facet of in vivo pretargeting: the ability to use radionuclides with half-lives that are normally incompatible with antibodies.

In this work, in response to these issues, we employed two radioisotopes of copper—positron-emitting ^{64}Cu and
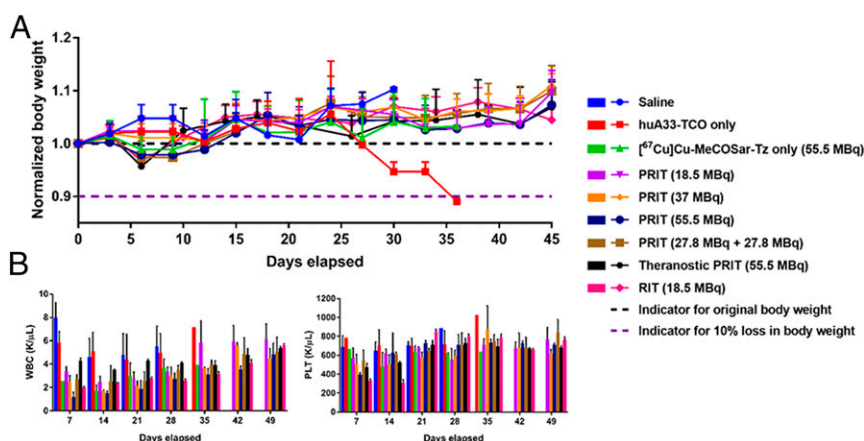
Fig. 6. Monitoring the tolerance of mice to ^{67}Cu-based endoradiotherapy. (*A*) Normalized body weight (*n* = 10) and (*B*) hematological values (*n* = 1 to 5) for the mice in the longitudinal therapy study. WBC: white blood cell count. PLT: platelet count. The data are represented as mean values ± SDs.

β-particle–emitting ^{67}Cu—to create a pair of chemically identical radioligands: [^{64}Cu]Cu-MeCOSar-Tz and [^{67}Cu]Cu-MeCOSar-Tz. The use of radioligands that are isotopologues has two principal advantages. First, the in vivo behavior of the two radioligands will be identical, facilitating the use of the former as a predictor of the biodistribution of the latter. Second, the use of only a single chemical species as a radioligand (Cu-MeCOSar-Tz) will simplify toxicological testing and streamline the regulatory review process as a whole.

In light of our previous work, the biodistribution data for pretargeting with huA33-TCO and [^{67}Cu]Cu-MeCOSar-Tz present relatively few surprises. Tumoral uptake of the radioligand is apparent at even the earliest time point and grows throughout the course of the experiment, suggesting that the ^{67}Cu-labeled tetrazine is clicking with both tumor-bound huA33-TCO and circulating immunoconjugate that subsequently accumulates in the xenograft. The [^{67}Cu]Cu-MeCOSar-Tz clears from the blood and healthy organs relatively quickly, ultimately yielding promising tumor-to-healthy organ activity concentration ratios across the board. From a dosimetry perspective, the ^{67}Cu-PRIT strategy produces significantly reduced individual organ dose rates compared to the directly radiolabeled ^{67}Cu-huA33. Decreases in radiation doses can also be seen when ^{67}Cu-PRIT is compared to ^{177}Lu-labeled huA33, arguably a more realistic comparison since ^{67}Cu is seldom used to label full-length IgG for the clinic. To wit, the radiation dose rate to the blood for ^{67}Cu-PRIT is estimated to be 5.9 cGy/MBq, compared to 71.3 cGy/MBq for ^{67}Cu-huA33 and 67.7 cGy/MBq for ^{177}Lu-huA33 (Fig. 3*B* and *SI Appendix,* Table S6). Unfortunately, however, ^{67}Cu-PRIT also produces lower radiation doses to the tumor compared to directly labeled ^{67}Cu-huA33 and ^{177}Lu-huA33. As a result, the therapeutic indices for pretargeting are generally comparable to those of the traditional radioimmunoconjugates for most organs, and the critical tumor-to-blood therapeutic index for ^{67}Cu-PRIT (9.7 with a 72-h interval) is only marginally higher than that of ^{67}Cu-huA33 (8.1) and lies below that of ^{177}Lu-huA33 (18.6). This is an area that can be improved upon in the future. Optimizing the timing of the methodology and the doses of each of the components, for example, could improve therapeutic indices by increasing dose rates to the tumor and/or decreasing dose rates to healthy organs. Furthermore, our laboratory and others have also explored the use clearing agents as a means of reducing activity concentrations in the blood and healthy organs; however, clearing agents, while effective, would inevitably add yet another element of complexity to an already complex system.

The longitudinal therapy studies provide a platform to compare the efficacy of the various treatment strategies. Most importantly, all of the radiotherapy cohorts exhibit statistically significant differences in mean survival time compared to all of the control cohorts. In addition, a statistically significant dose-dependent response was observed for the low-, medium-, and high-dose PRIT cohorts. Intriguingly, while a statistically significant difference was not observed between the median survival times of the 55.5-MBq PRIT (200 d) and fractionated PRIT (189 d) cohorts, four mice in the latter regrew tumors over the course of the experiment compared to only one in the former. This phenomenon likely stems from the fact that the fractionated dose cohort did not receive its second 27.8-MBq dose (bringing the total up to 55.5 MBq) until 120 h after the administration of huA33-TCO, potentially lowering the overall radiation dose to the tumor. Nonetheless, the SPECT imaging results for the fractionated PRIT cohort clearly illustrate that the second administration of the radioligand increases the activity concentration in the tumor, suggesting that fractionated dosing could be a viable approach if optimized further. The mean survival time of the 55.5-MBq PRIT cohort is also matched by the cohort receiving 18.5 MBq of [^{67}Cu]Cu-huA33. The RIT cohort, however, does outperform the PRIT cohort receiving an identical 18.5-MBq dose, a result that is not surprising given the higher dose rate of RIT to tumor tissue. It is worth noting that equal dose comparisons were not performed between RIT and PRIT at the 37.0- and 55.5-MBq levels because the literature suggests that these doses of a ^{67}Cu-labeled antibody would cause acute radiation toxicity in mice (71). Finally, the body-weight monitoring and blood analysis generally suggest that all of the radiotherapeutic strategies are well tolerated, although slight yet temporary dips in the body weight, WBC count, and platelet count were observed in the cohorts of mice receiving higher radiation doses.

Despite the promise of ^{67}Cu-PRIT alone, the most exciting results from this study arguably arise from the experiments featuring our theranostic approach to PRIT. In the longitudinal therapy study, the cohort receiving theranostic $^{64/67}$Cu-PRIT had a mean survival time of >200 d, equal to that of the groups treated with 55.5-MBq PRIT and 18.5-MBq RIT. That said, four mice in the theranostic PRIT cohort exhibited tumor regrowth—three to the point of being killed and one only slightly—compared to one in the single-dose PRIT group that received the same dose of [^{67}Cu]Cu-MeCOSar-Tz. In light of our previous finding that the administration of one radioligand does not impede the uptake of a second (48), it is unlikely that this phenomenon is related to the use of two injections in the
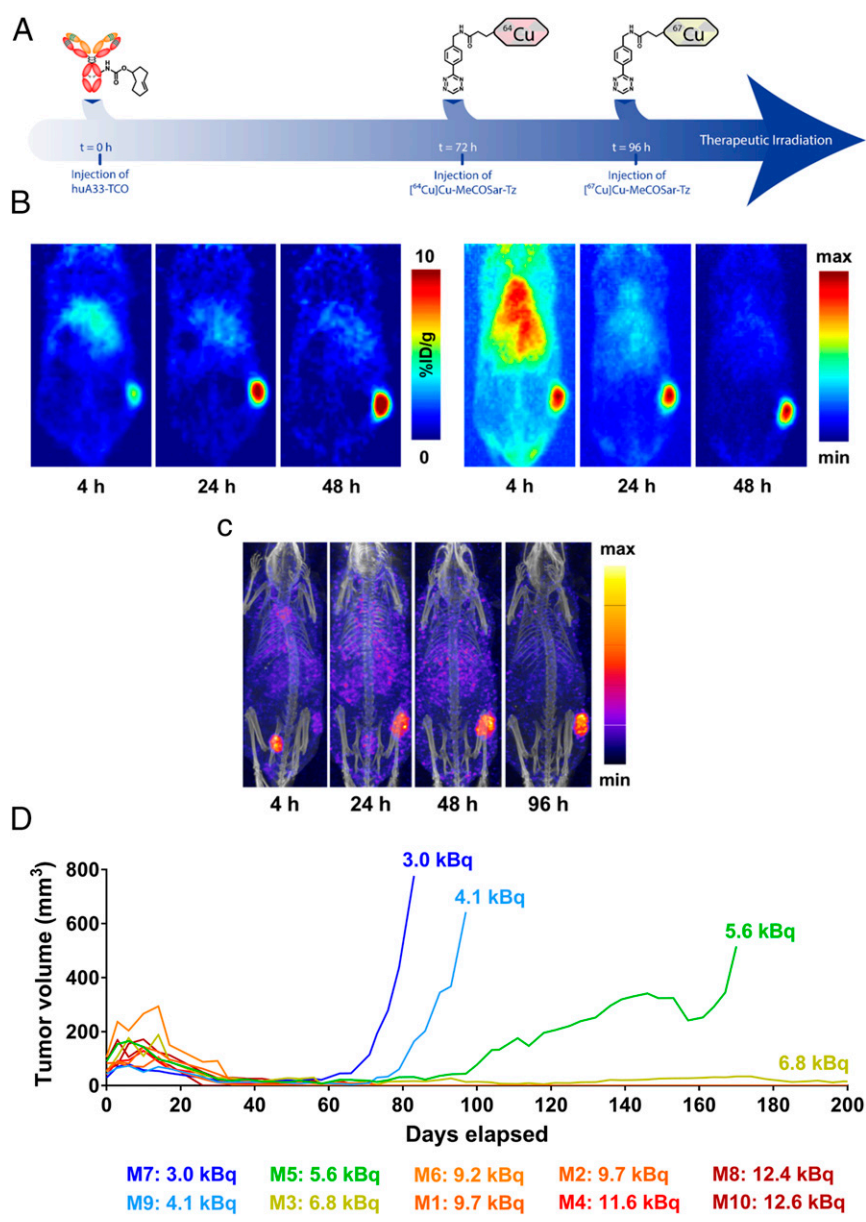
Fig. 7. PRIT with theranostic PET. (*A*) Schematic of the theranostic PRIT experiment. (*B*) Coronal slice and MIP PET images of a representative mouse in the theranostic cohort at 4, 24, and 48 h post injection of [^{64}Cu]Cu-MeCOSar-Tz. The coronal slices intersect the center of the tumor. (*C*) SPECT-CT MIP images of the same representative mouse from the theranostic cohort collected at 4, 24, 48, and 96 h after the administration of [^{67}Cu]Cu-MeCOSar-Tz. (*D*) The tumor volume of each animal in the theranostic cohort as a function of time. The amount of radioactivity at the center of the tumor was determined via region of interest (ROI) analysis of PET image slices acquired at 48 h post injection.

theranostic cohort. A more probable explanation may lie in the heterogeneity of the tumors or, more likely still, that the mice in the single-dose PRIT cohort received [^{67}Cu]Cu-MeCOSar-Tz 72 h after the injection of huA33-TCO while those in the theranostic group received the ^{67}Cu-labeled radioligand 96 h after the administration of the immunoconjugate. The most critical finding, however, is that the PET imaging results could have allowed us to predict which of the mice would experience tumor regrowth. The four mice with the lowest levels of radioactivity in the tumor in the 48-h PET scans (3.0, 4.1, 5.6, and 6.8 kBq) were those whose tumors regrew. In contrast, all of the other members of the cohort—whose xenografts contained >9.0 kBq of [^{64}Cu]Cu-MeCOSar-Tz—experienced complete and lasting shrinkage of their tumor tissue. In the end, while our previous work established the feasibility of dual radionuclide pretargeting, this investigation

goes two critical steps further: demonstrating the therapeutic efficacy of ^{67}Cu-PRIT and illustrating the usefulness of pretargeted ^{64}Cu-PET as a predictive indicator of response to ^{67}Cu-PRIT.

We believe that the data from this investigation lay out a clear road map for the incorporation of theranostic PET imaging into PRIT regimens. As pretargeted PET inches ever closer to the clinic—the first images from pancreatic cancer patients are expected in early 2021—one can easily envision how pretargeted imaging and therapy could be combined in the future: after the collection of initial PET scans, physicians could decide whether a patient is a suitable candidate for PRIT. If the tumoral standard uptake value (SUV) is above a predetermined threshold, the patient would then receive a dose of a therapeutic Tz radioligand. On the other hand, if the PET scan revealed insufficient uptake, the clinicians would pivot and pursue other therapeutic options.

Ultimately, we believe that this paradigm could be instrumental in the creation of safe and effective PRIT strategies for colorectal cancer, pancreatic cancer, and beyond.

Data Availability. All study data are included in the article and *SI Appendix*.

1. U. Eberlein, M. Cremonesi, M. Lassmann, Individualized dosimetry for theranostics: Necessary, nice to have, or counterproductive? *J. Nucl. Med.* **58**, 97S–103S (2017).
2. A. Yordanova *et al.*, Theranostics in nuclear medicine practice. *OncoTargets Ther.* **10**, 4821–4828 (2017).
3. H. Jadvar, X. Chen, W. Cai, U. Mahmood, Radiotheranostics in cancer diagnosis and management. *Radiology* **286**, 388–400 (2018).
4. J. R. Ballinger, Theranostic radiopharmaceuticals: Established agents in current use. *Br. J. Radiol.* **91**, 20170969 (2018).
5. A. G. Terwisscha van Scheltinga *et al.*, Preclinical efficacy of an antibody-drug conjugate targeting mesothelin correlates with quantitative ^{89}Zr-ImmunoPET. *Mol. Cancer Ther.* **16**, 134–142 (2017).
6. H. Cho *et al.*, A comparison of DFO and DFO* conjugated to trastuzumab-DM1 for complexing ^{89}Zr–In vitro stability and in vivo microPET/CT imaging studies in NOD/SCID mice with HER2-positive SK-OV-3 human ovarian cancer xenografts. *Nucl. Med. Biol.* **84-85**, 11–19 (2020).
7. N. Al-Saden, Z. Cai, R. M. Reilly, Tumor uptake and tumor/blood ratios for [^{89}Zr] Zr-DFO-trastuzumab-DM1 on microPET/CT images in NOD/SCID mice with human breast cancer xenografts are directly correlated with HER2 expression and response to trastuzumab-DM1. *Nucl. Med. Biol.* **67**, 43–51 (2018).
8. G. Gebhart *et al.*, Molecular imaging as a tool to investigate heterogeneity of advanced HER2-positive breast cancer and to predict patient outcome under trastuzumab emtansine (T-DM1): The ZEPHIR trial. *Ann. Oncol.* **27**, 619–624 (2016).
9. E. J. ter Weele *et al.*, Imaging the distribution of an antibody-drug conjugate constituent targeting mesothelin with ^{89}Zr and IRDye 800CW in mice bearing human pancreatic tumor xenografts. *Oncotarget* **6**, 42081–42090 (2015).
10. L. E. Lamberts *et al.*, ImmunoPET with anti-mesothelin antibody in patients with pancreatic and ovarian cancer before anti-mesothelin antibody-drug conjugate treatment. *Clin. Cancer Res.* **22**, 1642–1652 (2016).
11. P. Adumeau *et al.*, Site-specifically labeled antibody-drug conjugate for simultaneous therapy and ImmunoPET. *Mol. Pharm.* **15**, 892–898 (2018).
12. F. Bensch *et al.*, ^{89}Zr-atezolizumab imaging as a non-invasive approach to assess clinical response to PD-L1 blockade in cancer. *Nat. Med.* **24**, 1852–1858 (2018).
13. A. N. Niemeijer *et al.*, Whole body PD-1 and PD-L1 positron emission tomography in patients with non-small-cell lung cancer. *Nat. Commun.* **9**, 4664 (2018).
14. Y. Wang *et al.*, Dose escalation PET imaging for safety and effective therapy dose optimization of a bispecific antibody. *MAbs* **12**, 1748322 (2020).
15. J. Vento *et al.*, PD-L1 detection using ^{89}Zr-atezolizumab immuno-PET in renal cell carcinoma tumorgrafts from a patient with favorable nivolumab response. *J. Immunother. Cancer* **7**, 144 (2019).
16. C. G. England *et al.*, Preclinical pharmacokinetics and biodistribution studies of ^{89}Zr-labeled pembrolizumab. *J. Nucl. Med.* **58**, 162–168 (2017).
17. A. Kjaer, U. Knigge, Use of radioactive substances in diagnosis and treatment of neuroendocrine tumors. *Scand. J. Gastroenterol.* **50**, 740–747 (2015).
18. M. Schottelius *et al.*, Twins in spirit–Episode I: Comparative preclinical evaluation of [(^{68}Ga]DOTATATE and [(^{68}Ga]HA-DOTATATE. *EJNMMI Res.* **5**, 22 (2015).
19. A. Afshar-Oromieh *et al.*, The theranostic PSMA ligand PSMA-617 in the diagnosis of prostate cancer by PET/CT: Biodistribution in humans, radiation dosimetry, and first evaluation of tumor lesions. *J. Nucl. Med.* **56**, 1697–1705 (2015).
20. C. Kratochwil *et al.*, 225Ac-PSMA-617 for PSMA-targeted α-radiation therapy of metastatic castration-resistant prostate cancer. *J. Nucl. Med.* **57**, 1941–1944 (2016).
21. S. Lütje *et al.*, PSMA ligands for radionuclide imaging and therapy of prostate cancer: Clinical status. *Theranostics* **5**, 1388–1401 (2015).
22. K. Rahbar, A. Afshar-Oromieh, H. Jadvar, H. Ahmadzadehfar, PSMA theranostics: Current status and future directions. *Mol. Imaging* **17**, 1536012118776068 (2018).
23. J. Zang *et al.*, First-in-human study of ^{177}Lu-EB-PSMA-617 in patients with metastatic castration-resistant prostate cancer. *Eur. J. Nucl. Med. Mol. Imaging* **46**, 148–158 (2019).
24. S. M. Larson, J. A. Carrasquillo, N. K. Cheung, O. W. Press, Radioimmunotherapy of human tumours. *Nat. Rev. Cancer* **15**, 347–360 (2015).
25. W. K. Tsai, A. M. Wu, Aligning physics and physiology: Engineering antibodies for radionuclide delivery. *J. Labelled Comp. Radiopharm.* **61**, 693–714 (2018).
26. C. Bailly *et al.*, Immuno-PET for clinical theranostic approaches. *Int. J. Mol. Sci.* **18**, 57 (2016).
27. K. L. Moek *et al.*, Theranostics using antibodies and antibody-related therapeutics. *J. Nucl. Med.* **58**, 83S–90S (2017).
28. M. Altai, R. Membreno, B. Cook, V. Tolmachev, B. M. Zeglis, Pretargeted imaging and therapy. *J. Nucl. Med.* **58**, 1553–1559 (2017).
29. A. Rondon, F. Degoul, Antibody pretargeting based on bioorthogonal click chemistry for cancer imaging and targeted radionuclide therapy. *Bioconjug. Chem.* **31**, 159–173 (2020).
30. E. J. L. Stéen *et al.*, Pretargeting in nuclear imaging and radionuclide therapy: Improving efficacy of theranostics and nanomedicines. *Biomaterials* **179**, 209–245 (2018).
31. M. L. Blackman, M. Royzen, J. M. Fox, Tetrazine ligation: Fast bioconjugation based on inverse-electron-demand Diels–Alder reactivity. *J. Am. Chem. Soc.* **130**, 13518–13519 (2008).
32. R. Rossin *et al.*, Highly reactive trans-cyclooctene tags with improved stability for Diels–Alder chemistry in living systems. *Bioconjug. Chem.* **24**, 1210–1217 (2013).
33. R. Rossin *et al.*, In vivo chemistry for pretargeted tumor imaging in live mice. *Angew. Chem. Int. Ed.* **49**, 3375–3378 (2010).
34. B. M. Zeglis *et al.*, A pretargeted PET imaging strategy based on bioorthogonal Diels–Alder click chemistry. *J. Nucl. Med.* **54**, 1389–1396 (2013).
35. R. Rossin, S. M. van Duijnhoven, T. Läppchen, S. M. van den Bosch, M. S. Robillard, Trans-cyclooctene tag with improved properties for tumor pretargeting with the Diels–Alder reaction. *Mol. Pharm.* **11**, 3090–3096 (2014).
36. B. M. Zeglis *et al.*, Optimization of a pretargeted strategy for the PET imaging of colorectal carcinoma via the modulation of radioligand pharmacokinetics. *Mol. Pharm.* **12**, 3575–3587 (2015).
37. J. L. Houghton *et al.*, Pretargeted immuno-PET of pancreatic cancer: Overcoming circulating antigen and internalized antibody to reduce radiation doses. *J. Nucl. Med.* **57**, 453–459 (2016).
38. J. P. Meyer *et al.*, (18)F-Based pretargeted PET imaging based on bioorthogonal Diels–Alder click chemistry. *Bioconjug. Chem.* **27**, 298–301 (2016).
39. B. E. Cook *et al.*, Pretargeted PET imaging using a site-specifically labeled immunoconjugate. *Bioconjug. Chem.* **27**, 1789–1795 (2016).
40. P. Adumeau *et al.*, A pretargeted approach for the multimodal PET/NIRF imaging of colorectal cancer. *Theranostics* **6**, 2267–2277 (2016).
41. J. P. Meyer *et al.*, Exploring structural parameters for pretargeting radioligand optimization. *J. Med. Chem.* **60**, 8201–8217 (2017).
42. E. M. F. Billaud *et al.*, Pretargeted PET imaging using a bioorthogonal ^{18}F-labeled trans-cyclooctene in an ovarian carcinoma model. *Bioconjug. Chem.* **28**, 2915–2920 (2017).
43. A. Rondon *et al.*, Antibody PEGylation in bioorthogonal pretargeting with trans-cyclooctene/tetrazine cycloaddition: In vitro and in vivo evaluation in colorectal cancer models. *Sci. Rep.* **7**, 14918 (2017).
44. O. Keinänen *et al.*, Pretargeting of internalizing trastuzumab and cetuximab with a ^{18}F-tetrazine tracer in xenograft models. *EJNMMI Res.* **7**, 95 (2017).
45. B. E. Cook, R. Membreno, B. M. Zeglis, Dendrimer scaffold for the amplification of in vivo pretargeting ligations. *Bioconjug. Chem.* **29**, 2734–2740 (2018).
46. J. P. Meyer *et al.*, Bioorthogonal masking of circulating antibody-TCO groups using tetrazine-functionalized dextran polymers. *Bioconjug. Chem.* **29**, 538–545 (2018).
47. D. Summer *et al.*, Pretargeted imaging with gallium-68-improving the binding capability by increasing the number of tetrazine motifs. *Pharmaceuticals (Basel)* **11**, 102 (2018).
48. O. Keinänen *et al.*, Dual radionuclide theranostic pretargeting. *Mol. Pharm.* **16**, 4416–4421 (2019).
49. P. M. R. Pereira *et al.*, Temporal modulation of HER2 membrane availability increases pertuzumab uptake and pretargeted molecular imaging of gastric tumors. *J. Nucl. Med.* **60**, 1569–1578 (2019).
50. J. L. Houghton *et al.*, Establishment of the in vivo efficacy of pretargeted radioimmunotherapy utilizing inverse electron demand Diels–Alder click chemistry. *Mol. Cancer Ther.* **16**, 124–133 (2017).
51. M. A. Shah *et al.*, Metal-free cycloaddition chemistry driven pretargeted radioimmunotherapy using α-particle radiation. *Bioconjug. Chem.* **28**, 3007–3015 (2017).
52. R. Membreno, B. E. Cook, K. Fung, J. S. Lewis, B. M. Zeglis, Click-mediated pretargeted radioimmunotherapy of colorectal carcinoma. *Mol. Pharm.* **15**, 1729–1734 (2018).
53. R. Membreno *et al.*, Toward the optimization of click-mediated pretargeted radioimmunotherapy. *Mol. Pharm.* **16**, 2259–2263 (2019).
54. S. Poty *et al.*, Leveraging bioorthogonal click chemistry to improve ^{225}Ac-radioimmunotherapy of pancreatic ductal adenocarcinoma. *Clin. Cancer Res.* **25**, 868–880 (2019).
55. A. Rondon *et al.*, Pretargeted radioimmunotherapy and SPECT imaging of peritoneal carcinomatosis using bioorthogonal click chemistry: Probe selection and first proof-of-concept. *Theranostics* **9**, 6706–6718 (2019).
56. N. A. Smith, D. L. Bowers, D. A. Ehst, The production, separation, and use of ^{67}Cu for radioimmunotherapy: A review. *Appl. Radiat. Isot.* **70**, 2377–2383 (2012).
57. F. Kraeber-Bodéré *et al.*, Tumor immunotargeting using innovative radionuclides. *Int. J. Mol. Sci.* **16**, 3932–3954 (2015).
58. N. M. Di Bartolo, A. M. Sargeson, T. M. Donlevy, S. V. Smith, Synthesis of a new cage ligand, SarAr, and its complexation with selected transition metal ions for potential use in radioimaging. *Dalton Trans.* ((15), 2303–2309 (2001).
59. M. S. Cooper *et al.*, Comparison of (64)Cu-complexing bifunctional chelators for radioimmunoconjugation: Labeling efficiency, specific activity, and in vitro/in vivo stability. *Bioconjug. Chem.* **23**, 1029–1039 (2012).
60. C. Cullinane *et al.*, Peptide receptor radionuclide therapy with ^{67}Cu-CuSarTATE is highly efficacious against a somatostatin positive neuroendocrine tumor model. *J. Nucl. Med.*, jnumed.120.243543 (2020).

61. C. Biggin, E. van Dam, M. Harris, M. Parker, G. Schembri, Estimating external exposure from patients after treatment with Cu-67 SARTATE. *J. Nucl. Med.* **60**, 1624a (2019).

62. J. K. Heath *et al.*, The human A33 antigen is a transmembrane glycoprotein and a novel member of the immunoglobulin superfamily. *Proc. Natl. Acad. Sci. U.S.A.* **94**, 469–474 (1997).

63. S. Welt *et al.*, Phase I/II study of iodine 125-labeled monoclonal antibody A33 in patients with advanced colon cancer. *J. Clin. Oncol.* **14**, 1787–1797 (1996).

64. A. M. Scott *et al.*, A phase I trial of humanized monoclonal antibody A33 in patients with colorectal carcinoma: Biodistribution, pharmacokinetics, and quantitative tumor uptake. *Clin. Cancer Res.* **11**, 4810–4817 (2005).

65. M. E. Ackerman *et al.*, A33 antigen displays persistent surface expression. *Cancer Immunol. Immunother.* **57**, 1017–1027 (2008).

66. K. Alt *et al.*, Single-chain antibody conjugated to a cage amine chelator and labeled with positron-emitting copper-64 for diagnostic imaging of activated platelets. *Mol. Pharm.* **11**, 2855–2863 (2014).

67. B. M. Paterson *et al.*, PET imaging of tumours with a ^{64}Cu labeled macrobicyclic cage amine ligand tethered to Tyr3-octreotate. *Dalton Trans.* **43**, 1386–1396 (2014).

68. E. Gourni *et al.*, Copper-64 labeled macrobicyclic sarcophagine coupled to a GRP receptor antagonist shows great promise for PET imaging of prostate cancer. *Mol. Pharm.* **12**, 2781–2790 (2015).

69. R. J. Hicks *et al.*, ^{64}Cu-SARTATE PET imaging of patients with neuroendocrine tumors demonstrates high tumor uptake and retention, potentially allowing prospective dosimetry for peptide receptor radionuclide therapy. *J. Nucl. Med.* **60**, 777–785 (2019).

70. S. M. van Duijnhoven *et al.*, Diabody pretargeting with click chemistry in vivo. *J. Nucl. Med.* **56**, 1422–1428 (2015).

71. G. L. DeNardo *et al.*, Efficacy and toxicity of [67]Cu-2IT-BAT-Lym-1 radioimmunoconjugate in mice implanted with human Burkitt's lymphoma (Raji). *Clin. Cancer Res.* **3**, 71–79 (1997).

MEDICAL SCIENCES